IJE TRANSACTIONS B: Applications Vol. 39, No. 05, (May 2026) 1047-1062

International Journal of Engineering

Journal Homepage: www.ije.ir

Physics-Informed Neural Networks Techniques for Analyzing Forced Vibrations of Simply Supported Beams Featuring Variable Cross-Sections

S. M. Sahebdad[a], M. Eftekhari*[a], M. Eftekhari[b]

[a] *Department of Mechanical Engineering, Shahid Bahonar University of Kerman, Kerman, Iran*
[b] *Department of Computer Engineering, Shahid Bahonar University of Kerman, Kerman, Iran*

PAPER INFO

Paper history:
Received 31 March 2025
Received in revised form 17 May 2025
Accepted 06 June 2025

Keywords:
Free and Forced Vibration
Isotropic Beam
Variable Cross Section
Physics-informed Neural Networks
Galerkin Method

ABSTRACT

This research explores the forced vibrations of isotropic beams with variable cross-sections, modeled by the Euler-Bernoulli beam theory. Using Hamilton's principle, the governing partial differential equations are derived, and the complex vibrational behaviors were analyzed. By introducing physics-informed neural networks (PINNs) as an innovative, mesh-free solution technique, the study highlights their ability to provide rapid and precise results by integrating physical laws directly into the machine learning framework. Compared to traditional methods like finite element (FEM) or finite difference schemes, PINNs significantly streamline the computational process by eliminating the need for mesh generation, which simplifies implementation and reduces computational effort, validation with the 6th-order Galerkin method and FEM confirms the high accuracy and efficiency of the proposed approach for analyzing vibrations in beams with varying cross-sections. Overall, this work enhances the application of PINNs in vibration assessment and offers valuable insights for optimizing design and performance across diverse engineering domains, including structural and mechanical systems.

doi: *10.5829/ije.2026.39.05b.01*

Graphical Abstract

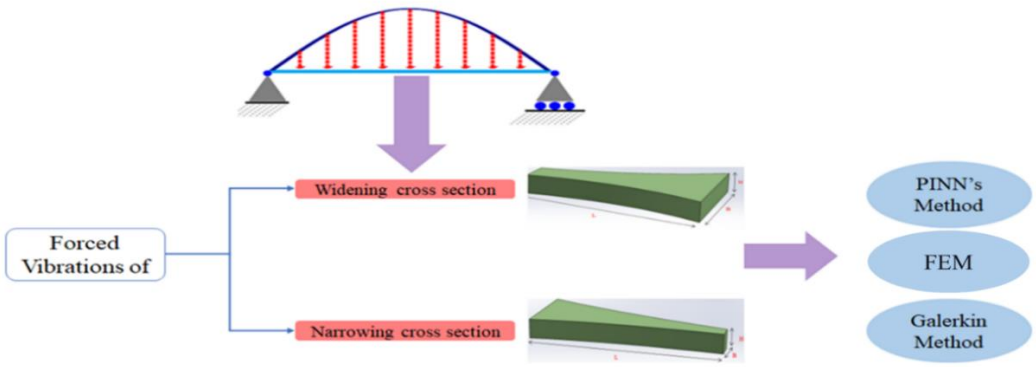

1. INTRODUCTION

Isotropic beams stand out for their uniform mechanical properties in all directions, which is why they are widely used in various engineering fields. This uniformity allows these beams to consistently respond to stresses and deformations, making them particularly vital in sectors such as aerospace (1, 2). As highlighted in a

*Corresponding author email: mo.eftekhari@uk.ac.ir (M. Eftekhari)

Please cite this article as: Sahebdad SM, Eftekhari M, Eftekhari M. Physics-Informed Neural Networks Techniques for Analyzing Forced Vibrations of Simply Supported Beams Featuring Variable Cross-Sections. International Journal of Engineering, Transactions B: Applications. 2026;39(05):1047-62.

recent study by Li and Shen (3), they proposed an optimized seismic design method for civil structures combined with robotic construction system technology. Their study emphasized the importance of integrating kinematic analysis of installation robots with internet-based seismic monitoring data to identify hidden safety hazards and implement effective safety management. This approach addresses the challenges of manual installation in high-rise projects and leverages smart robotic equipment to improve construction accuracy, reduce errors, and enhance the seismic resistance of structures. The results include the determination of optimal safety weights and thresholds, demonstrating a significant improvement in the strength and safety of the structures.

The reliability of isotropic beams under various loading conditions underscores their superiority in the design and construction of structures requiring high performance and strength, as exemplified by a very practical and recent study by Makrup et al. (4) conducted a study comparing structural responses derived from probabilistic seismic hazard analysis (PSHA) with those obtained using design spectral ground motion approaches. Their research highlights the importance of integrating these methodologies to achieve a comprehensive understanding of seismic impacts on structures. Results indicate that the structural responses predicted by both methods are quite similar, supporting the reliability of using either approach in seismic design.

Their work emphasized the value of combining probabilistic and deterministic methods to enhance earthquake-resistant design and ensure structural safety in seismic-prone areas., which illustrates the importance of these beams in various applications.

Despite extensive research conducted on the analysis of transverse vibrations of isotropic beams, Canales et al. (5) Moreno-García et al. (6), Azzara, Ghugal et al. (7), Ghugal et al. (8)) there is an urgent need to investigate non-uniform beams that possess variable mass and stiffness distributions. These non-uniform beams can exhibit unique characteristics that significantly differ from their isotropic counterparts. The analysis of vibrations in beams with variable cross-sections not only addresses diverse engineering needs but also contributes to the optimization of design and performance.

This study emphasizes the examination of transverse vibrations in isotropic beams featuring non-uniform cross-sections in this regard, the Euler-Bernoulli beam theory acts as the foundational framework for analysis, simplifying the governing equations of beam motion under various loading conditions. To derive the relevant equations, Hamilton's principle is utilized, which allows for the extraction of a partial differential equations (PDEs) governing the motion of the beam. The application of Hamiltonian mechanics in structural analysis contributes to a more comprehensive understanding of energy distribution throughout the system, thereby simultaneously addressing both kinetic and potential energy. The resulting PDEs encompasses the complexities of the transverse vibration states of the beam while considering variations in the cross-sectional geometry.

In recent years, considerable progress has been achieved in the field of machine learning, particularly concerning neural networks. Physics-informed neural networks (PINNs) idea, initially introduced by Raissi et al. (9) are recognized as a major advancement in numerical solution methods that have created a link between neural networks and engineering physical models. These networks derive the necessary information through differential equations, boundary conditions, and initial conditions governing engineering systems.

The primary incentive for employing PINNs is their capacity to deliver significantly simpler solutions for a variety of problems, requiring very few training data points and operating at a much faster pace compared to traditional numerical approaches such as Finite Element Method (FEM) (10, 11), Finite Difference Method (FDM) (12, 13) Galerkin method discussed by Wang and Wu (14), and other computational techniques (15).

As a mesh-free approach, PINNs can solve different issues several times faster than these conventional methods. In this research, the outcomes derived from PINNs are verified and contrasted with the results obtained via Galerkin method.

Various issues have been studied using PINNs yielding very suitable responses, and different studies in the field of vibrations can be addressed.

Chen et al. (16) explored an enhanced Physics-Informed Neural Network (PINN) approach for structural vibration analysis in "long-duration" simulations. They presented a significant technical hurdle that remains unaddressed within the realm of PINNs. The performance of both the standard PINN (STD-PINN) and conventional time-marching PINN (CT-PINN) techniques in solving vibration equations, especially free-vibration equations, tends to decline over extended simulation periods. This method tackles structural vibration challenges across successive time intervals by implementing four crucial strategies: normalizing the spatiotemporal domain for each interval, employing a reactivating optimization algorithm, utilizing transfer learning, and adopting the sine activation function. The findings reveal that the Advanced time-marching PINN (AT-PINN) method provides accurate solutions while maintaining a reduced computational expense, even throughout prolonged simulations.

Bazmara et al. (17) framework for PINNs was created to explore the nonlinear bending of three-dimensional (3D) functionally graded (FG) beams. The researchers established a mathematical model employing Euler-

Bernoulli beam theory in conjunction with an inhomogeneous beam model, confirming their results against findings from the finite difference method. Additionally, the PINNs technique has demonstrated the ability to forecast the nonlinear bending of the system up to 37 times more swiftly than traditional numerical methods.

In another work, Bazmara et al. (18) PINNs framework has been developed to investigate the nonlinear buckling characteristics of a three-dimensional (3D) functionally graded (FG) porous slender beam supported by a Winkler-Pasternak foundation. This PINN framework utilizes data derived from the governing differential equations of the beam system, along with boundary condition information, to ascertain the critical nonlinear buckling load. The findings from the PINNs framework are corroborated against results obtained from the generalized differential quadrature method (GDQM), illustrating that the proposed PINNs accurately capture the nonlinear buckling behavior of 3D FG porous slender beams. Furthermore, the PINNs approach forecasts nonlinear buckling behavior up to 71 times faster than conventional numerical methods.

Models utilizing PDEs to represent Euler-Bernoulli and Timoshenko beams on a Winkler foundation were executed through a causal physics-informed neural network (PINN) combined with transfer learning, as demonstrated by Kapoor et al. (19). The main contribution of this paper lies in the creation of a causality-respecting PINN loss function specifically designed for structural engineering, combined with transfer learning to improve the adaptability of PINNs in simulating the dynamics of beams on elastic foundations. Numerical tests on Euler-Bernoulli beam demonstrate the efficacy of the proposed approach across various initial conditions, including cases with noise in the initial data. Additionally, the method's capabilities are illustrated for the Timoshenko beam over an expanded spatial and temporal range.

Moreover, Kapoor et al. (20) developed an innovative framework that utilizes PINNs to model complex structural systems consisting of single and double beams, applying Euler-Bernoulli and Timoshenko theories. In this framework, the double beams rest on a Winkler foundation. The results suggest that PINNs offer a promising solution for tackling challenges associated with engineering structures and machinery involving beam systems.

Söyleyici and Ünver (21) investigated an innovative framework based on PINN for solving the theory of free vibrations of Euler-Bernoulli beams and demonstrates its capabilities in identifying damping constants. The results obtained indicate that the use of multi-scale Fourier features and a neural tactile kernel can enhance prediction accuracy in beam vibration analysis, particularly at high frequencies.

Teloli et al. (22) developed an innovative method that utilizes PINNs to tackle inverse problems in structural analysis. This technique is particularly applied to the fourth-order PDEs derived from Euler-Bernoulli theory to evaluate beam deflection and determine critical structural parameters such as damping and elastic modulus. The approach incorporates PDEs into the loss function of the neural network during training, ensuring adherence to physics-based constraints. This method streamlines intricate structural assessments, even in cases where boundary conditions are ambiguous. The proposed technique successfully extracts structural properties using experimental data and confirms its accuracy against sophisticated methodologies.

Despite existing research, Physics-Informed Neural Networks (PINNs) have significant shortcomings. Therefore, this study investigates the forced vibration problem in Euler-Bernoulli beams with variable cross-sections using Physics-Informed Neural Networks. Furthermore, the obtained responses will be validated against results from the Galerkin method and Finite Element Analysis.

In this study, the deep learning library PyTorch version 2.5.0 was used to construct a Physics-Informed Neural Network (23-25). This library is comprehensive in the field and facilitates the development of Physics-Informed Neural Networks.

The main objective of this research is to develop a framework of Physics-Informed Neural Networks (PINNs) for investigating the vibrations of Euler-Bernoulli beams with variable cross-sections. This study notably differs from other research in the field of Physics-Informed Neural Networks dealing with beam vibrations, as it examines beams with variable cross-sections under forced vibration scenarios. Moreover, the responses obtained through the developed Physics-Informed Neural Networks are validated using the Galerkin method and Finite Element Analysis. This approach is very simple, as it does not require discretizing derivatives, approximating a set of basics functions to satisfy boundary conditions, or solving complex frequency equations. It also eliminates the need for refining the number of elements, the complexities of weak form meshing and time-space discretization, and solving systems of equations with various numerical methods; it only requires the differential equation and its boundary and initial conditions to solve the problem with the network. The clear distinction of this study lies in the construction and design of an efficient and fast network for solving forced vibration problems for beams with variable cross-sections. This study can provide a fast, efficient, and less cumbersome process for solving such problems.

Therefore, this work advances the field by combining forced vibration analysis, variable cross-sections, and PINNs in a way that is not fully replicated in the related

literature (15-23).

More details about this research are explained in the following sections: Section 2 is devoted to the mathematical formulation. The principle of Physics-Informed Neural Networks (PINNs) is introduced in section 3. Section 4 pertains to the Finite Element Method theory. Results and analyses are described in section 5. Finally, section 6 concludes the paper.

2. MATHEMATICAL MODELING

This study investigates a structural element consisting of an isotropic beam with a specified length L, oriented along the x-axis. The beam has a variable cross-section with a width B along the y-axis and a height H along the z-axis, as illustrated in Figure 1. Figure 1.c, a simply supported beam subjected to a prescribed load is depicted. additionally, Figures 1.a and 1.b respectively show an isotropic wide-section beam and an isotropic narrow-section beam.

According to the Euler-Bernoulli beam theory, the relationship between axial strain displacement can be expressed as follows:

$$\varepsilon_{xx} = -z\frac{\partial^2 w}{\partial x^2} + \frac{\partial u}{\partial x} + \frac{1}{2}\left(\frac{\partial w}{\partial x}\right)^2 \quad (1)$$

In the context of an isotropic beam, where u and w represent the axial and transverse displacements, respectively, the normal stress can be derived using the principles of linear elastic constitutive law:

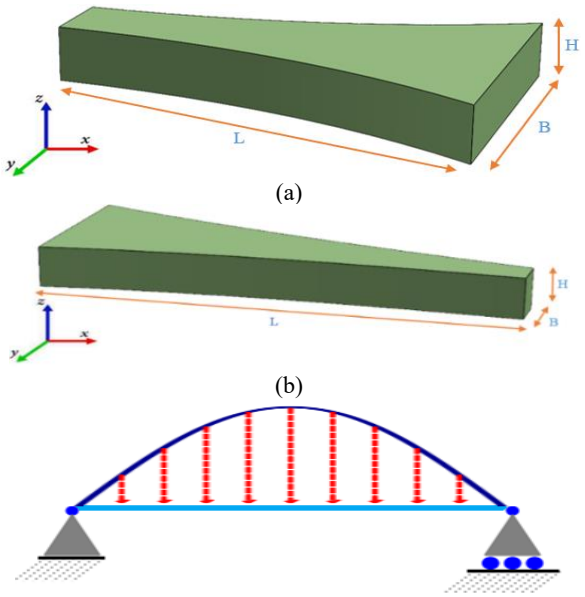

Figure 1. Schematic of a simply supported beam with variable cross sections a) widening b) narrowing

$$\sigma_{xx} = E\left(-z\frac{\partial^2 w}{\partial x^2} + \frac{\partial u}{\partial x} + \frac{1}{2}\left(\frac{\partial w}{\partial x}\right)^2\right) \quad (2)$$

where E represents Young's modulus. Variation of potential energy is explained as:

$$\delta U = \int_V \sigma_{xx}\delta\varepsilon_{xx}\, dV = \int_0^L \int_A \sigma_{xx}\, \delta\left(-z\frac{\partial^2 w}{\partial x^2} + \frac{\partial u}{\partial x} + \frac{1}{2}\left(\frac{\partial w}{\partial x}\right)^2\right) dA dx = \int_0^L N_{xx}\delta\left(\frac{\partial u}{\partial x} + \frac{1}{2}\left(\frac{\partial w}{\partial x}\right)^2\right) - M_{xx}\delta\frac{\partial^2 w}{\partial x^2}\, dx \quad (3)$$

In which, A refers to the beam's cross-sectional area, while N_{xx} and M_{xx} denote the axial load and moment of bending per unit length, respectively:

$$N_{xx} = \int_A \sigma_{xx}\, dA \quad (4)$$

$$M_{xx} = \int_A \sigma_{xx}\, z\, dA \quad (5)$$

The variational representation of the external force (δw_{nc}) is expressed as follows:

$$\delta w_{nc} = \int_0^L P sin\left(\frac{\pi x}{L}\right)\cos(\Omega t)\, \delta w dx \quad (6)$$

In Equation 6, P, L, and Ω represent the load, the length of the beam, and the frequency, respectively. variation of kinetic energy (δT):

$$\delta T = \int_0^L \frac{1}{2}\rho A(x)\left(\left(\frac{\partial u}{\partial t}\right)^2 + \left(\frac{\partial w}{\partial t}\right)^2\right) = \int_0^L \rho A(x)\frac{\partial u}{\partial t}\delta\frac{\partial u}{\partial t}dx + \int_0^L \rho A(x)\frac{\partial w}{\partial t}\delta\frac{\partial w}{\partial t}dx \quad (7)$$

Hamilton's principle was employed to derive the governing equations for beams with non-uniform cross-sections., which are expressed as follows:

$$\int_{t_1}^{t_2}(\delta T - \delta U + \delta W_{nc})\, dt = 0 \quad (8)$$

By substituting Equations 3, 6, and 7 into Equation 8 and employing integration by parts with respect to the variables, the following results are obtained, leading to two equations for lateral and axial displacements:

$$\delta u: \frac{\partial N_{xx}}{\partial x} - \rho A(x)\frac{\partial^2 u}{\partial t^2} = 0 \quad (9)$$

$$\delta w: N_{xx}\frac{\partial^2 w}{\partial x^2} - \frac{\partial N_{xx}}{\partial x}\frac{\partial w}{\partial x} + \frac{\partial^2 M_{xx}}{\partial x^2} + \rho A(x)\frac{\partial^2 w}{\partial t^2} + P sin\left(\frac{\pi x}{L}\right)cos(\Omega t) = 0 \quad (10)$$

From Equation 9, conclude $\frac{\partial N_{xx}}{\partial x} = \rho A(x)\frac{\partial^2 u}{\partial t^2}$. By assuming the axial vibration is much smaller than the lateral vibration, the time-dependent longitudinal component of Equation 9 can be disregarded:

$$\frac{\partial N_{xx}}{\partial x} = 0, \quad (11)$$

The displacement $u(x,t)$ is determined as follows:

$$\frac{\partial}{\partial x}\left[\int_A \sigma_{xx}\ dA\right]=0\rightarrow\frac{\partial}{\partial x}\left[\int_A\left(E\ \left(-z\frac{\partial^2 w}{\partial x^2}+\ \frac{\partial u}{\partial x}+\ \frac{1}{2}\left(\frac{\partial w}{\partial x}\right)^2\right)\right)dA\right]=0\rightarrow\int_A z\ dA=0,\frac{\partial}{\partial x}\left[EA\left(\frac{\partial u}{\partial x}+\ \frac{1}{2}\left(\frac{\partial w}{\partial x}\right)^2\right)\right]=0,\rightarrow,$$

$$\frac{\partial}{\partial x}\left[EA\left(\frac{\partial u}{\partial x}+\frac{1}{2}\left(\frac{\partial w}{\partial x}\right)^2\right)\right]=0,\rightarrow,EA\left(\frac{\partial u}{\partial x}+\ \frac{1}{2}\left(\frac{\partial w}{\partial x}\right)^2\right)=c_1$$

$$EA\left(u+\int_0^x\frac{1}{2}\left(\frac{\partial w}{\partial x}\right)^2dx\right)=c_1x+c_2,\quad(12)$$

$$u(0,t)=0\rightarrow c_2=0\ ,u(L,t)=0,\rightarrow$$

$$c_1=\frac{EA}{L}\left(\int_0^L\frac{1}{2}\left(\frac{\partial w}{\partial x}\right)^2dx\right),\rightarrow u(x,t)=\frac{c_1}{EA}x-\int_0^x\frac{1}{2}\left(\frac{\partial w}{\partial x}\right)^2dx,\rightarrow N_{xx}=\frac{EA}{L}\left(\int_0^L\frac{1}{2}\left(\frac{\partial w}{\partial x}\right)^2dx\right),$$

$$u(x,t)=\frac{c_1}{EA}x-\int_0^x\frac{1}{2}\left(\frac{\partial w}{\partial x}\right)^2dx$$

$$N_{xx}=\frac{EA}{L}\left(\int_0^L\frac{1}{2}\left(\frac{\partial w}{\partial x}\right)^2dx\right)$$

By substituting Equation 11 in Equation 10 and neglecting the nonlinear cubic terms:

$$\frac{\partial^2 M_{xx}}{\partial x^2}+\rho A(x)\frac{\partial^2 w}{\partial t^2}-Psin\left(\frac{\pi x}{L}\right)cos(\Omega t)=0\quad(13)$$

$\frac{\partial^2 M_{xx}}{\partial x^2}$ is presented for a variable cross section as follows:

$$M_{xx}=\ EI(x)\frac{\partial^2 w}{\partial x^2},\rightarrow\frac{\partial^2 M_{xx}}{\partial x^2}=EI''(x)\frac{\partial^2 w}{\partial x^2}+2EI'(x)\frac{\partial^3 w}{\partial x^3}+\ EI(x)\frac{\partial^4 w}{\partial x^4}\quad(14)$$

By substituting Equation 14 into Equation 13 one obtains:

$$EI(x)\frac{\partial^4 w}{\partial x^4}+\ 2EI'(x)\frac{\partial^3 w}{\partial x^3}+\ EI''(x)\frac{\partial^2 w}{\partial x^2}+\rho A(x)\frac{\partial^2 w}{\partial t^2}=\ Psin\left(\frac{\pi x}{L}\right)cos(\Omega t)\quad(15)$$

Equation 16 is utilized to define dimensionless variables, allowing the governing equation to be represented in a dimensionless form as follows:

$$\hat{t}=\frac{1}{L^2}\sqrt{\frac{EI_0}{\rho A_0}},\hat{x}=\frac{x}{L},\widehat{w}=\frac{w}{L},\hat{I}=\frac{I}{I_0},\hat{P}=\frac{PL^3}{\hat{A}EI_0},\quad\widehat{\Omega}=\Omega L^2\sqrt{\frac{\rho A_0}{EI_0}},\hat{A}=\frac{A}{A_0}\quad(16)$$

y substituting dimensionless variables in Equation 16 into Equation 15 one obtains:

$$\frac{\hat{I}(\hat{x})}{\hat{A}(\hat{x})}\frac{\partial^4\widehat{w}}{\partial\hat{x}^4}+\ 2L\frac{\hat{I}'(\hat{x})}{\hat{A}(\hat{x})}\frac{\partial^3\widehat{w}}{\partial\hat{x}^3}+\ L^2\frac{\hat{I}''(\hat{x})}{\hat{A}(\hat{x})}\frac{\partial^2\widehat{w}}{\partial\hat{x}^2}+\frac{\partial^2\widehat{w}}{\partial\hat{t}^2}=\hat{P}\sin(\pi\hat{x})\,cos\left(\widehat{\Omega}\hat{t}\right)\quad(17)$$

In this study, the boundary conditions are defined as simply supported on both ends, as indicated in Equation 18.

$$\widehat{w}\ (0,\hat{t})=0\qquad\widehat{w}\ (1,\hat{t})=0$$

$$\frac{\partial^2\widehat{w}(0,\hat{t})}{\partial\hat{x}^2}=0\qquad\frac{\partial^2\widehat{w}(1,\hat{t})}{\partial\hat{x}^2}=0\quad(18)$$

3. PRINCIPLE OF PHYSICS-INFORMED NEURAL NETWORKS (PINNs)

Physics-informed neural networks (PINNs) signify a notable progression in the convergence of machine learning and scientific computing. In this essay, essential concepts that form the basis of PINNs will be outlined, focusing on three primary aspects: 3.1 Fundamentals of PINNs, 3.2 Automatic Differentiation in PINNs, and 3.3 Adaptive Activation functions**.** By integrating incorporate fundamental physical principles directly into the training process, PINNs enhance model accuracy and generalization. This approach allows for more reliable predictions in complex systems where traditional machine learning methods may struggle. Figure 2 shows the Framework of a PINN approach.

3. 1. Fundamental of PINNs Examine a typical PDE system parameterized by using Λ, the solution can be found $j(x,t)$ defined across a domain $\Gamma\subset\mathbb{R}$ with $x=(x_1,\cdots,x_e)$ and t representing time (9, 26). This system can be expressed in partial differential equations that characterize the behavior of the solution $j(x,t)$ across the spatial domain and over time, allowing for various boundary and initial conditions to be applied.

$$F(x,t;\frac{\partial j}{\partial x_1},\dots\frac{\partial j}{\partial x_e},\frac{\partial j}{\partial x_1};\frac{\partial j}{\partial t},\frac{\partial^2 j}{\partial t^2};\frac{\partial j}{\partial x_1\partial x_1},\dots,\frac{\partial j}{\partial x_1\partial x_e},\dots\frac{\partial j}{\partial x_1\partial x_e};\frac{\partial j}{\partial t\,\partial x_1},\dots,\frac{\partial j}{\partial t\,\partial x_e};\dots,\Lambda)=0$$

$$j(x,t)=\alpha_0(x,t)\quad(19)$$

$$j\ (x,t)=\ \alpha_\Gamma(0,t)=0$$

$$x\in\ \Gamma,x\in\ \partial\Gamma$$

Let Γ represent the spatiotemporal domain, while $\partial\Gamma$ indicates the boundary. The spatial coordinate is denoted by $x\ \in\Gamma$, and F signifies the residual of the partial differential equation (PDE), which includes the differential operators. $[\frac{\partial j}{\partial x_1},\dots,\frac{\partial j}{\partial x_e},\dots,\frac{\partial j}{\partial t},\frac{\partial^2 j}{\partial t^2}]$; $\Lambda=[\Lambda_1,\Lambda_2,\cdots]$. The parameters of the partial differential equation (PDE) include $j(x,t)$, which denotes the solution of the PDE given certain boundary conditions $\alpha_0(x,t)$. These boundary conditions can be of different types, including Robin, Neumann, and Dirichlet, in addition to the initial conditions $\alpha_\Gamma(0,t)$.

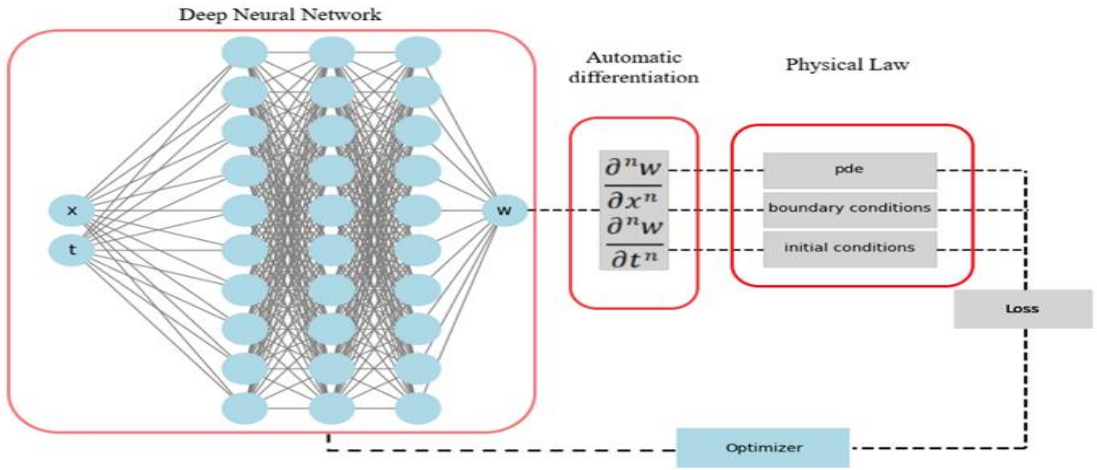

Figure 2. Framework of a PINN approach

In the realm of PINNs, a feed-forward neural network with multiple hidden layers is designed to estimate the solution of a partial differential equation (PDE) over time. It does this by using spatial coordinates as inputs and producing an output vector that matches the dimensionality of the problem, $j(x,t)$, as Shown in Figure 2. In Equation 20, the term h^0 within the equation incorporates the variables x and t, reflecting the input variable from the initial layer. This input is then transmitted to the subsequent layer as Z^1, t in the neural network, represented by Equations 20 and 21 below:

$$Z^1 = w^1 h^0 + b^1,\ O^1 = \psi(Z^1) \quad \text{For } k=1$$
$$Z^k = w^k O^{k-1} + b^k \quad \text{For } 2 \le k \le L\text{-}1 \tag{20}$$

$$O^k = \psi(Z^k) \quad \text{For } 2 \le k \le L\text{-}1$$
$$O^L = w^L O^{L-1} + b^L \quad \text{For } k = L \tag{21}$$

Where L represents a neural network with L-layer, and L refers to the total count of hidden layers; w^k and α^k signify the weights and bias terms for the k^{th} layer; ψ denotes a nonlinear activation function. Z^k and O^k depict the input and output of the activation function ψ for the k^{th} layer respectively. From the sequence of Relations 20 and 21, it can be observed that O^k is used as the input for the k+1 layer.

PINNs address the specified system of PDE system outlined in Equation 21 by refining the problem through the iterative modification of the trainable model parameters, which encompass w^k and α^k, with the goal of minimizing the loss function $J(\theta)$ as specified in Equation 22.

$$J(\theta) = \lambda_{pde} L_{pde}(\theta) + \lambda_{ic} L_{ic}(\theta) + \lambda_{bc} L_{bc}(\theta) \tag{22}$$

where

$$L_{pde} = \frac{1}{N_{pde}} \sum_{i=1}^{N_{pde}} \left(\mathcal{F}\left(\hat{x}^i{}_{pde}, \hat{t}^i{}_{pde} \right) \right)^2 \tag{23}$$

$$L_{ic} = \frac{1}{N_{ic}} \sum_{i=1}^{N_{ic}} \left(\hat{w}\left(\hat{x}^i{}_{ic}, 0 \right) - K^i{}_0\left(\hat{x}^i{}_{ic} \right) \right)^2 + \left(\frac{\partial \hat{w}(\hat{x}^i{}_{ic}, 0)}{\partial t} - K^i{}_1\left(\hat{x}^i{}_{ic} \right) \right)^2 \tag{24}$$

$$L_{bc} = \frac{1}{N_{bc}} \sum_{i=1}^{N_{bc}} \left(\hat{w}\left(\hat{x}^i{}_{bc}, \hat{t}^i{}_{bc} \right) - \hat{w}^i \right)^2 + + \left(\frac{\partial^n \hat{w}(\hat{x}^i{}_{bc}, \hat{t}^i{}_{bc})}{\partial x^n} - \frac{\partial^n \hat{w}^i}{\partial x^n} \right)^2 \tag{25}$$

In this context, λ_{pde}, λ_{ic} and λ_{bc} represent the weights. L_{pde} evaluates the residuals of the governing equations. $\Theta = \{w^k, b^k\}_{k=1}^{L}$ stands for trainable parameters. Moreover, to comply with L_{ic} and L_{bc} are the initial conditions for the predictions of PINNs align with the data and boundary conditions, initial conditions are incorporated. Automatic differentiation (AD) is employed to compute the derivatives of the neural network and its components through the application of the chain rule Equation 18. Specifically, the loss function in Equation 22 is characterized as sampling the Mean Square Error (MSE) in Equation 23, where the term $F(x,t)$ pertains to the PDE equation, and N_{pde} signifies the number of training points in the PDE domain. In Equation 24, $k_0(x)$ indicates the actual initial value, while $k_1(x)$ represents the actual initial velocity, with N_{ic} denoting the number of training points for the initial conditions. Additionally, Equation 25 generally illustrates various types of boundary conditions, which may exhibit different states based on the problem's requirements, with N_{bc} indicating the number of training points for the boundary conditions. Typically, in the MSE

approach, the predicted value of the grid is subtracted from the actual value and raised to the power of two.

Two different optimizers were used independently to fine-tune the weights and biases of each layer, resulting in varying outcomes, with one demonstrating superior performance. The first optimizer, which is more commonly used, and the second optimizer, which we used to solve the problem, are compared in performance in Figures 4 and 5. Figure.3 related to the optimizer ADAM Mehmood et al. (27) and Figure 4 to the optimizer L-BFGS Tong et al. (28) which has shown significantly better performance.

Establishing an appropriate loss function is paramount in the development of neural network algorithms, as it encapsulates the fundamental physical laws governing the problem at hand. This study formulates the loss function by integrating PDEs, initial conditions, and boundary conditions. Furthermore, it explores the interplay between these elements and their impact on the model's performance. Ultimately, this framework aspires to enhance the precision and dependability of the solutions generated by the neural network.

3. 2. Automatic Differentiation (AD) in PINNs

Automatic Differentiation (AD) is pivotal for computing partial derivatives, a fundamental step in formulating the loss function outlined in Equation 21. By leveraging the chain rule integrated into machine learning frameworks like PyTorch, AD facilitates the direct computation of derivatives of outputs concerning the inputs to the network within the computational graph. In contrast to traditional numerical methods, AD eliminates the necessity of calculating discretization and truncation errors by deriving derivatives through explicit expressions. It is important to recognize that neural networks are utilized to parameterize the partial differential equations (PDEs) and their derivatives, leading to what are termed generalization and optimization errors, influenced by the training dataset and the optimizer, respectively. The schematic framework of PINNs and their critical components employed in this study are depicted. A physical problem is examined, as illustrated in various sections of Figure 5.

3. 3. Adaptive Activation Function (AAF)

As detailed in sections (3.1) and (3.2), the derivative of the loss function depends on the optimization parameters, highlighting the importance of the activation function. Different activation functions, such as sine and hyperbolic tangent (tanh), and others, are utilized within the PINNs framework, tailored to address specific challenges. Although the training initially employed a standard tanh function, it encountered convergence issues with the loss function. To address this challenge, this study introduces an adaptive activation function, incorporating a hyperparameter β into the activation mechanism, as delineated in Equation 26. This approach effectively mitigates the convergence difficulties experienced by Jagtap et al. (29, 30).

This approach enables greater flexibility and adaptability during training. By incorporating the hyperparameter, more stable convergence behavior across various problem types is anticipated. The findings indicate a significant enhancement in the efficiency and effectiveness of the model, ultimately leading to better performance in solving the target equations.

$$O^k = \psi(\beta Z^k) = \frac{e^{\beta Z^k} - e^{-\beta Z^k}}{e^{\beta Z^k} + e^{-\beta Z^k}} \tag{26}$$

In this approach, the parameter β is determined through the simultaneous reduction of the loss function along with the weights and biases. This methodology substantially improves the accuracy of the model. and therefore, it leads to the optimization of $\theta = \{w^k, b^k, \beta\}_{k=1}^{L}$ as:

$$\theta^* = agrmin_{\beta \in \Lambda \geq 0}(J(\theta)) \tag{27}$$

Additionally, the hyper-parameter β is adjusted along with weights and biases as follows:

$$\theta^{i+1} = \theta^i - \alpha \nabla_\theta J^i(\theta) \tag{28}$$

where $0 < \alpha \leq 1$ is the learning rate to regulate the impact of the learning factor on the activation Function 25, which is responsible for to achieve convergence to minima, one should scale the hyper-parameter β through a multiplier. Additionally, this adjustment can enhance the model's performance during training.$\eta > 1$, which produces a new activation function.

$$O^k = \psi(\eta \beta Z^k) \tag{29}$$

Comprehensive and detailed information regarding the impact of this parameter η can be found in the literature [29,30].

4. FINITE ELEMENT METHOD

The Finite Element Method (FEM) is a powerful numerical technique for solving partial differential equations (PDEs) governing dynamic systems, such as forced vibrations of beams in structural engineering. This section presents a comprehensive mathematical framework for analyzing forced vibrations of an Euler-Bernoulli beam with variable cross-sectional area $A(x)$, variable moment of inertia $I(x)$, and constant damping, using FEM. The formulation includes the derivation of the weak form, spatial discretization, assembly of system matrices, and numerical solution techniques. Detailed explanations are provided for element discretization, degrees of freedom (DOFs), and shape functions, ensuring clarity for applying FEM to a general forced

vibration problem. the sections include 4.1 Governing Equation, 4.2 Weak Form Derivation, 4.3 Element Discretization and Degrees of Freedom, 4.4 Shape Functions, 4.5 Element Matrices and Force Vector, 4.6 Global Assembly.

4. 1. Governing Equation The governing PDE for an Euler-Bernoulli beam undergoing forced vibrations in a one-dimensional domain $x \in [0, L]$ over time $t \in [0, T]$ is:

$$\frac{\partial^2}{\partial x^2}\left(EI(x)\frac{\partial^2 w(x,t)}{\partial x^2}\right) + \rho A(x)\frac{\partial^2 w(x,t)}{\partial t^2} + c\frac{\partial w(x,t)}{\partial t} = f(x,t) \quad (30)$$

where: $w(x,t)$ transverse displacement of the beam, E Young's modulus, I(x)moment of inertia, varying along the beam length, A(x) cross-sectional area, varying along the beam length, ρ mass density (constant), c constant damping coefficient per unit length, $f(x,t)$ external forcing function, $x \in [0, L]$ spatial coordinate, $t \in [0,T]$ time. The first term represents bending stiffness, the second term is the inertial force, and the third term accounts for viscous damping (constant). The forcing function f (x,t) drives the forced vibration response. Boundary Conditions: For generality, consider the supported boundary conditions that are in Equation 18, although the framework can be adapted for other conditions, Initial Conditions

$$w(x,0) = w_0(x)\ , \frac{\partial w(x,0)}{\partial t} = v_0(x) \quad (31)$$

where $w_0(x)$ and $v_0(x)$ are the initial displacement and velocity distributions, respectively.

4. 2. Weak Form Derivation To apply FEM, the strong form of the PDE is converted into a weak form by multiplying by a test function $v(x) \in H^2(x)$, satisfying the essential boundary conditions ($v(0) = v(L) = 0$), and integrating over the domain. The weak form is:

$$\int_0^L \left[\frac{\partial^2}{\partial x^2}\left(EI(x)\frac{\partial^2 w(x,t)}{\partial x^2}\right) + \rho A(x)\frac{\partial^2 w(x,t)}{\partial t^2} + c\frac{\partial w(x,t)}{\partial t} - f(x,t)\right] v(x)dx = 0 \quad (32)$$

this must hold for all test functions $v(x) \in H^2(x)$ satisfying the boundary conditions.

4. 3. Element Discretization and Degrees of Freedom The domain $[0,L]$ is discretized into n finite elements of equal length $h = \frac{L}{n}$, forming a mesh with nodes at $x_i = ih$ (for i=0,1,…,n). Each element spans $[x_e, x_e+h]$, where $x_e = eh$ for element e = 0,1,…,n−1.

The number of elements n is chosen to balance accuracy and computational efficiency; a larger n (smaller h) captures variations in $A(x)$ and $I(x)$ more accurately but increases computational cost. Each element has two nodes (one at each end), and each node has two degrees of freedom, displacement (w_i): the transverse displacement at node i, rotation ($\theta_i = \frac{\partial w_i}{\partial x}$): the slope of the displacement at node i.

Thus, each element has a total of four DOFs, represented by the element DOF vector:

$$q^e = [w_1, \theta_1, w_2, \theta_2]^T \quad (33)$$

where w_1, θ_1 are the displacement and rotation at the left node ($x = x_e$), and w_2, θ_2 are at the right node ($x = x_e + h$). For a mesh with n elements, there are n+1 nodes, resulting in 2(n+1) DOFs before applying boundary conditions.

4. 4. Shape Functions The displacement within an element is approximated using Hermitian shape functions, which ensure C^1continuity (continuity of displacement and its first derivative) across element boundaries, necessary for the fourth-order PDE. The displacement is expressed as follows:

$$w(x,t) \approx w_h(x,t) = N(x)\, q^e(t) \quad (34)$$

where $N(x) = [N_1(x), N_2(x), N_3(x), N_4(x)]$is the vector of shape functions. In local coordinates $\xi = \frac{x - x_e}{h}$ ($0 \le \xi \le 1$):

$$N_1(\xi) = 1 - 3\xi^2 + 2\xi^3 \qquad N_2(\xi) = h(\xi - 2\xi^2 + \xi^3)$$
$$N_3(\xi) = 3\xi^2 - 2\xi^3 \qquad N_4(\xi) = h(-\xi^2 + \xi^3) \quad (35)$$

These functions satisfy:

$$N_1(0) = 1\ , N_1(1) = 0, \frac{dN_1(0)}{d\xi} = 0, \frac{dN_1(1)}{d\xi} = 0$$

displacement at ξ= 0

$$N_2(0) = 0, N_2(1) = 0, \frac{dN_2(0)}{d\xi} = h, \frac{dN_2(1)}{d\xi} = 0$$

rotation at ξ= 0

$$N_3(0) = 0\ , N_3(1) = 1, \frac{dN_3(0)}{d\xi} = 0, \frac{dN_3(1)}{d\xi} = 0$$

displacement at ξ=1

$$N_4(0) = 0\ , N_4(0) = 0, \frac{dN_4(0)}{d\xi} = 0, \frac{dN_4(1)}{d\xi} = h$$

rotation at ξ= 1

The test function is similarly approximated:

$$v(x) = N(x)v^e \quad (36)$$

The Hermitian shape functions are cubic polynomials, ensuring that both w_h and $\frac{\partial w_h}{\partial x}$are continuous across elements, which is critical for modeling the beam's bending behavior.

4. 5. Element Matrices and Force Vector Substituting $w_h = N\, q^e$ and $v_h = N\, v^e$ into the weak form for an element spanning $[x_e, x_e+h]$, the element-level equations are derived. The cross-sectional area

$A(x)$ and moment of inertia $I(x)$ re-assumed to vary linearly within each element:

$$A(x) = A_1 + (A_2 - A_1)\xi$$
$$I(x) = I_1 + (I_2 - I_1)\xi \quad (37)$$

where $A_1 = A(x_e)$,$A_2 = A(x_e h)$,$I_1\ I(x_e)$ and $I_2 = I(x_e + h)$.Integrals are expressed in local coordinates ξ with $dx = hd\xi$.

The Stiffness Matrix:

$$\int_{x_e}^{x_e+h} EI(x)\frac{\partial^2 w_h}{\partial x^2}\frac{\partial^2 v_h}{\partial x^2}dx = v^{eT}\left(\int_{x_e}^{x_e+h} EI(x)\frac{d^2N^T}{dx^2}\frac{d^2N}{dx^2}dx\right)q^e \quad (38)$$

$$K^e = \int_{x_e}^{x_e+h} EI(x)\frac{d^2N^T}{dx^2}\frac{d^2N}{dx^2}dx$$

Since $\frac{d\xi}{dx} = \frac{1}{h}$, $\frac{d^2N}{dx^2} = \frac{1}{h^2}\frac{d^2N}{d\xi^2}$

$$\frac{d^2N_1}{d\xi^2} = -6 + 12\xi \qquad \frac{d^2N_2}{d\xi^2} = h(-4 + 6\xi)$$
$$\frac{d^2N_3}{d\xi^2} = 6 - 12\xi \qquad \frac{d^2N_4}{d\xi^2} = h(-4 + 6\xi) \quad (39)$$

$$K^e = \int_0^L E\,[I_1 + (I_2 - I_1)\xi]\frac{1}{h^3}$$
$$\begin{bmatrix}(-6+12\xi)^2 & h(-6+12\xi)(-4+6\xi) & \cdots \\ \vdots & h^2(-4+6\xi)^2 & \cdots \\ \vdots & \vdots & \ddots\end{bmatrix}d\xi \quad (40)$$

Due to the linear variation of $I(x)$, the integral is typically evaluated numerically using quadrature methods Gauss-Legendre with 3 points to compute the matrix entries accurately.

The damping Matrix (C^e) is obtained as: (c is constant)

$$\int_{x_e}^{x_e+h} c\frac{\partial w_h}{\partial t}v_h dx = v^{eT}\left(\int_{x_e}^{x_e+h} cN^T N dx\right)\dot{q}^e$$
$$C^e = c\int_{x_e}^{x_e+h} N^T N\,dx = ch\int_0^L N^T N\,d\xi \quad (41)$$

$$C^e = \frac{ch}{420}\begin{bmatrix}156 & 22h & 54 & -13h \\ 22h & 4h^2 & 13h & -3h^2 \\ 54 & 13h & 156 & -22h \\ -13h & -3h^2 & -22h & 4h^2\end{bmatrix} \quad (42)$$

The mass Matrix (M^e) is obtained as:

$$\int_{x_e}^{x_e+h}\rho A(x)\frac{\partial^2 w_h}{\partial t^2}v_h dx = v^{eT}\left(\int_{x_e}^{x_e+h}\rho A(x)N^T N dx\right)\ddot{q}^e$$
$$M^e = \int_{x_e}^{x_e+h}\rho A(x)N^T N dx = \int_0^L \rho[A_1 + (A_2 - A_1)\xi]N^T N\,hd\xi \quad (43)$$

$$M^e = \rho h\int_0^L [A_1 + (A_2 - A_1)\xi] \quad (44)$$

$$\begin{bmatrix}N_1N_1 & N_1N_2 & N_1N_3 & N_1N_4 \\ N_2N_1 & N_2N_2 & N_2N_3 & N_2N_4 \\ N_3N_1 & N_3N_2 & N_3N_3 & N_3N_4 \\ N_4N_1 & N_4N_2 & N_4N_3 & N_4N_4\end{bmatrix}d\xi$$

With linear variation in $A(x)$, this integral is also evaluated numerically using quadrature methods to account for the ξ-dependent term.

The Force Vector ($F^e(t)$) is obtained as:

$$F^e(t) = \int_{x_e}^{x_e+h} f(x,t)N^T dx = \int_{-1}^{1} f(x_e + h\gamma, t)N^T h d\gamma \quad (45)$$

Using three-point Gauss-Legendre quadrature:

$$\gamma_i = \left[-\sqrt{\frac{3}{5}}, 0, \sqrt{\frac{3}{5}}\right] \qquad \omega_i = \left[\frac{5}{9}, \frac{8}{9}, \frac{5}{9}\right] \quad (46)$$

$$F^e(t) = \sum_{i=1}^{3}\omega_i\ f(x_e + h\gamma_i, t)N^T(\gamma_i)h \quad (47)$$

4. 6. Global Assembly The global stiffness (K), damping (C), mass (M), and force ($F(t)$) matrices are assembled by summing contributions from all elements. For n elements, there are $n + 1$ nodes and $2(n + 1)$ DOFs before boundary conditions. The DOFs for element eee are mapped as:

$$\text{Dofs} = [2e\ , 2e + 1\ , 2(e + 1), 2(e + 1) + 1] \quad (48)$$

Simply supported boundary conditions $w(0, t) = w(L, t) = 0$ are enforced by eliminating displacement DOFs at $x = 0$ $(index\ 0)$ and $x = L$ $(index\ 2n + 1)$, reducing the system to$K_{red}, C_{red}, M_{red}$ and F_{red} .

The Global finite element equation" The global finite element equation for the reduced system is:

$$M_{red}\ \ddot{q}_{red}(t) + C_{red}\dot{q}_{red}(t) + K_{red}q_{red}(t) = F_{red}(t) \quad (49)$$

In this study, Equation 52 given next section is solved using fourth-order Runge-Kutta method.

5. RESULTS AND DISCUSSIONS

In this section, the forced vibrations of a beam with variable cross-sections are investigated using Physics-Informed Neural Networks (PINNs), and the results are validated using the Galerkin and finite element methods. This study extracts results related to the forced vibrations of a beam with variable cross-section from subsection 5.1 and employs the PINNs method. Furthermore, the findings are compared with classical methods to ensure their accuracy and reliability. To optimize the accuracy and convergence of the numerical solution, hyperparameters were selected through trial and error, and the network was trained with different architectures to select the most optimal network for this problem. Regarding the selection of the network architecture,

various architectures were used, but a satisfactory response was not obtained. Therefore, to increase the convergence speed, an adaptive activation function was used to increase the convergence speed by creating adaptive changes in the slope of the activation function. However, to understand precisely the hyperparameter choices offered, the following problem is selected, where $\hat{C}$ is a dimensionless damping coefficient.

$$\frac{\partial^4 \hat{w}}{\partial x^4} + \frac{\partial^2 \hat{w}}{\partial t^2} + \hat{c}\frac{\partial \hat{w}}{\partial t} = \hat{P}\sin(\pi \hat{x})\, cos(\hat{\Omega}\hat{t}) \tag{50}$$

$$\hat{c} = \frac{c\, l}{EI_0\sqrt{\frac{EI_0}{\rho A_0}}} \tag{51}$$

This problem is subsequently investigated using Physics-Informed Neural Networks under specified boundary conditions Equation 18 and the initial conditions laid out in Equation 52.

$$\hat{w}(\hat{x}, 0) = 0$$
$$\frac{\partial \hat{w}(\hat{x}, 0)}{\partial t} = 0 \tag{52}$$

Initially, the problem was examined using a conventional activation function in conjunction with two optimization algorithms, ADAM and LBFGS. It is worth noting that a random dataset was used in this study to solve all problems. This dataset consists of 1600 points., 1600 points have been included, consisting of N_{pde}= 1000 number of training points in the PDE domain, N_{ic} = 200 number of training points initial conditions and N_{bc}= 400 number of training points boundary conditions, as shown in Figure 3.

However, the results were unsatisfactory. Subsequently, an approach utilizing an adaptive activation function was adopted, resulting in a significant improvement in outcomes. The network was then trained with various architectures, as shown in Table 1. Figure 4 illustrates the impact of the adaptive activation function on the network's performance, which is revealing that LBFGS significantly outperforms ADAM, regardless of whether adaptive or non-adaptive activation functions are employed. The introduction of the adaptive activation function notably enhanced the effectiveness of the LBFGS optimizer, leading to its continued use in this study. The learning rate for the ADAM optimizer is set at to 1e-4, while for the LBFGS optimizer, it is set at to 0.1. The training parameters include a maximum of 50,000 evaluations and a maximum of 1 iteration. It is important to note that the final loss values reported in Table 1 are influenced by the use of the adaptive activation function. Figures 5 and 6 display the loss evolution during training with the adaptive activation function for both optimizers: ADAM exhibits significant fluctuations, whereas LBFGS demonstrates minimal fluctuations, converging more rapidly and smoothly.

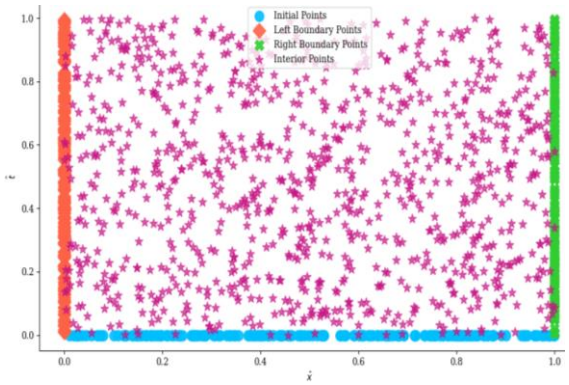

Figure 3. Data for learning beam parameters

TABLE 1. PINN Hyperparameters Across Different Cases

Architecture	Hidden layers N_h	Neuron layers N_n	Scale factor η	Final Loss Value
Model A	4	60	10	4.00e-6
Model B	8	80	10	3.65e-6
Model C	4	100	10	3.25e-6
Model D	3	100	10	3.18e-6

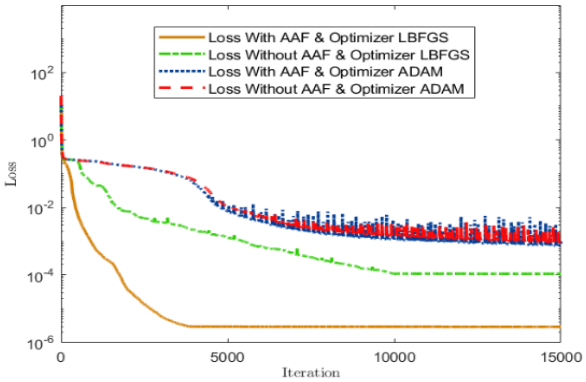

Figure 4. Impact of Activation Function Adaptivity on Optimization Efficiency with Adam and LBFGS

Based on all the results obtained throughout the training process of this study, the LBFGS optimizer and model architecture D will be utilized to analyze vibrations.

Now that the hyperparameters and optimizer of the designed network architecture have been set, we will examine the response obtained from solving problem in Equation 50. This solution has been validated with another issue resolved using Physics-Informed Neural Networks (PINNs) Chen et al. (16). As shown in Figure 7, the obtained solutions are in complete agreement with each other, and there are no significant errors. Additionally, Figure 7 includes higher-dimensional parameters.

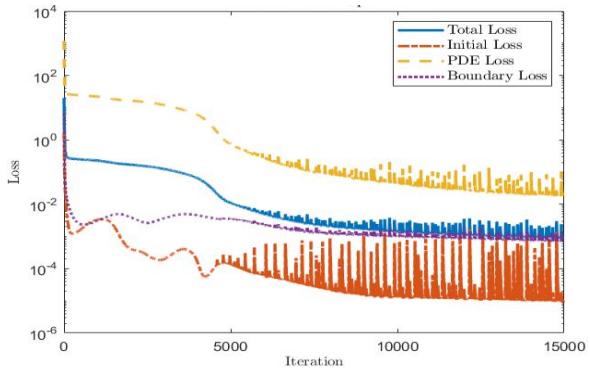

Figure 5. Training Loss Components: PDE, Initial Condition, and Boundary Condition with Adam Optimizer

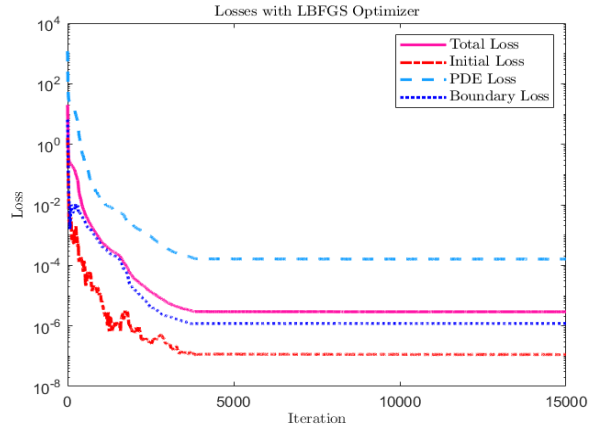

Figure 6. Training Loss Components Using LBFGS Optimizer: PDE, Initial Condition, and Boundary Condition

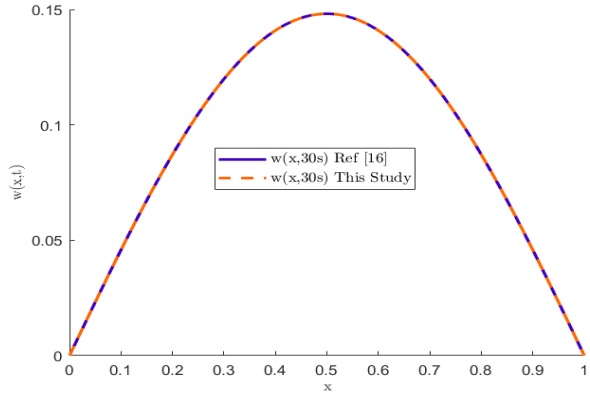

Figure 7. Comparison of responses from Chen et al. [16] and the PINNs method. Complete agreement indicates accuracy

In this study, the deep learning library PyTorch version 2.5.0 was used to construct a Physics-Informed Neural Network. This library is comprehensive in the field and facilitates the development of Physics-Informed Neural Networks. Also, a free Google Colab account with a T4 graphics processor, 16 GB of graphics memory, and 12 GB of RAM was utilized for conducting experiments.

After adjusting the hyperparameters according to the physical parameter issue, assuming that the height remains constant while the width changes $\hat{I}(\hat{x})= \hat{A}(\hat{x})$ in Table 2, and the curvature will be examined. specifically in section 5.1 concerning forced vibration analysis.

5. 1. Forced Vibration Analysis In this section, the analysis of forced vibrations is examined. is conducted based on the dimensionless parameters defined in Equation 14. The values are L = 1 m, P = 1.68 $\frac{N}{m}$, $\Omega = 6.0721\pi\ Hz$, $\rho A_0 = 0.1\frac{kg}{m}$ and EI_0= 0.16 $\frac{N}{m^2}$. By substituting these values into the parameters defined in Equation 16, the forced vibrations are examined according to Table 2.

It is assumed that the height remains constant, while the width changes exponentially ($e^{\delta_i x}$). Here, δ_i is a dimensionless scaling coefficient specified in Table 2. The initial conditions are outlined in Equation 52.

It is noteworthy that the validation conducted in this study was performed using two numerical methods: the sixth-order Galerkin method and finite element analysis with 22 elements. Ultimately, the system of equations was solved using the fourth-order Runge-Kutta method.

The absolute error was also calculated by comparing the results obtained from the finite element method with those obtained from the Physics-Informed Neural Networks (PINNs), which will be explained in detail below.

It is noteworthy that all graphs in this section represent dimensionless parameters.

$$\frac{\hat{I}(\hat{x})}{\hat{A}(\hat{x})}\frac{\partial^4\hat{w}}{\partial\hat{x}^4} + 2\frac{\hat{I}'(\hat{x})}{\hat{A}(\hat{x})}\frac{\partial^3\hat{w}}{\partial\hat{x}^3} + \frac{\hat{I}''(\hat{x})}{\hat{A}(\hat{x})}\frac{\partial^2\hat{w}}{\partial\hat{x}^2} + \frac{\partial^2\hat{w}}{\partial\hat{t}^2} = \hat{P}sin(\pi\hat{x})\,cos(\hat{\Omega}\hat{t}) \quad (53)$$

The effect of beam curvature, represented as $\delta_1 = 0$, illustrates the fixed bending patterns at various stages under applied forces, particularly in the context of forced vibrations. As shown in Figure 8, the maximum deflection consistently occurs at the center (1/2) of the beam, where both ends exhibit the same stiffness due to external loading. These observations highlight the intrinsic symmetry in the bending behavior of beams with uniform cross-sections under external forces. Following these findings, a comparison of beam behavior under different levels of applied force will be conducted. Figure 9 also depicts the behavior of this beam and its vibration

TABLE 2. Mechanical parameters for bending analysis

Mechanical parameters	$\hat{I}(\hat{x})$	$\hat{A}(\hat{x})$	δ_1	δ_2	δ_3	$\hat{P}$	$\hat{\Omega}$
Values	$e^{\delta_i\hat{x}}$	$e^{\delta_i\hat{x}}$	0	0.5	-0.5	$\frac{10.5}{e^{\delta_i\hat{x}}}$	4.8π

amplitude, which can be further analyzed using the finite element method as illustrated in Figure 10. The absolute error depicted in Figure 11 between these two methods, which is less than 0.07%, indicates that the PINNs method is reliable.

The impact of beam expansion with a profile of $\delta_2 = 0.5$ is described. We evaluate the deflection of the beam at various stages of bending, as shown in Figure 12. Observations indicate that the deflection shifts from the center towards the left, revealing a difference in stiffness between the two sides of the beam. Consequently, the maximum deflection is observed on the stiffer side, leading to a reduction in the vibration amplitude compared to beams with $\delta_1 = 0$. This reduction can be seen in Figure 13, along with the harmonic shape, and a comparison with the finite element method in Figure 14 shows that the results of both are identical. In Figure 15. The absolute error between the finite element results and PINNs is approximately 0.34%.

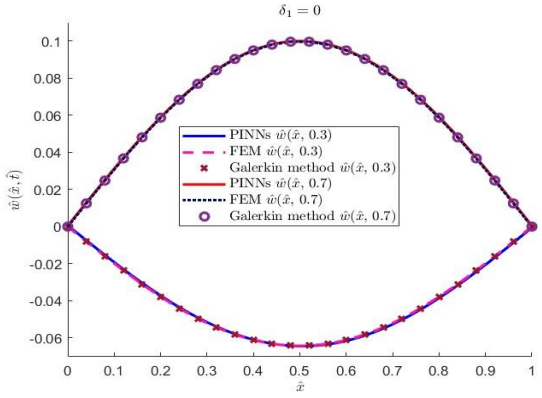

Figure 8. Forced vibration of beam with constant cross section area ($\delta_1 = 0$). comparison of the Galerkin, FEM and predicted PINNs

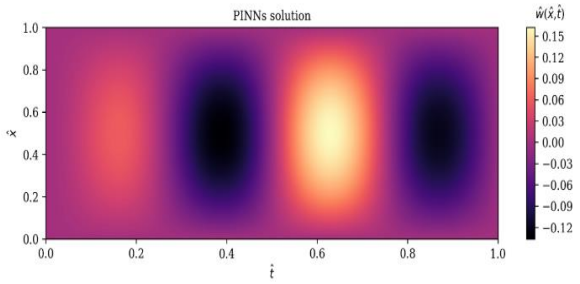

Figure 9. Transverse displacement of beam with constant cross section area ($\delta_1 = 0$). color bar represents PINNs solution

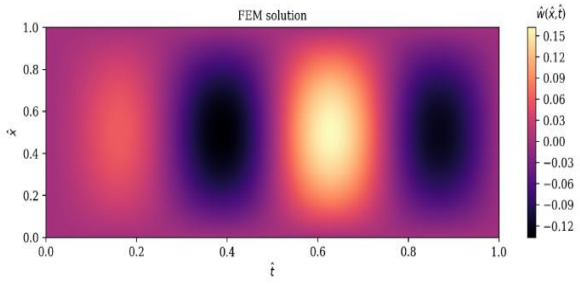

Figure 10. Transverse displacement of beam with constant cross section area ($\delta_1 = 0$). color bar represents FEM solution

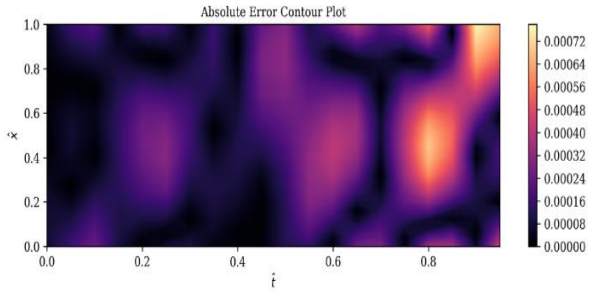

Figure 11. Absolute error in prediction PINNs & FEM $|w_{Pred} - w_{FEM}|$ for beam with constant cross section area ($\delta_1 = 0$)

between the two sides of the beam. Consequently, the maximum deflection is observed on the stiffer side, leading to a reduction in the vibration amplitude compared to beams with $\delta_1 = 0$. This reduction can be seen in Figure 13, along with the harmonic shape, and a comparison with the finite element method in Figure 14 shows that the results of both are identical. In Figure 15. The absolute error between the finite element results and PINNs is approximately 0.34%.

The impact of beam expansion with a profile of $\delta_2 = 0.5$ is described. We evaluate the deflection of the beam at various stages of bending, as shown in Figure 12. Observations indicate that the deflection shifts from the center towards the left, revealing a difference in stiffness between the two sides of the beam. Consequently, the maximum deflection is observed on the stiffer side, leading to a reduction in the vibration amplitude compared to beams with $\delta_1 = 0$. This reduction can be seen in Figure 13, along with the harmonic shape, and a comparison with the finite element method in Figure 14 shows that the results of both are identical. In Figure 15, the absolute error between the finite element results and PINNs is approximately 0.34%.

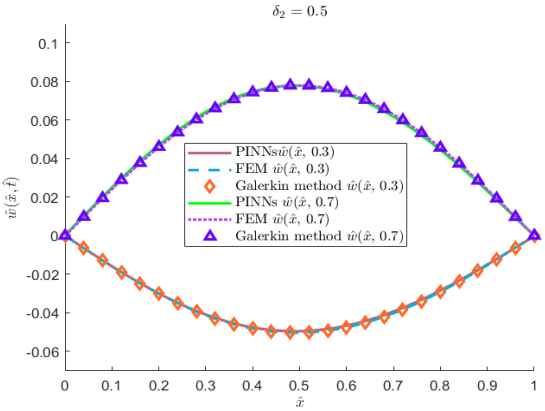

Figure 12. Forced vibration of beam with variable cross section area ($\delta_2 = 0.5$). comparison of the Galerkin, FEM and PINNs

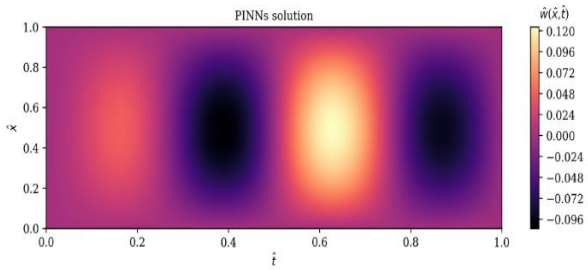

Figure 13. Transverse displacement of beam with constant cross section area ($\delta_2 = 0.5$). color bar represents PINNs solution

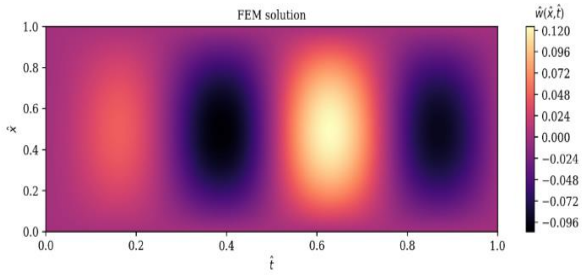

Figure 14. Transverse displacement of beam with constant cross section area ($\delta_2 = 0.5$). color bar represents FEM solution

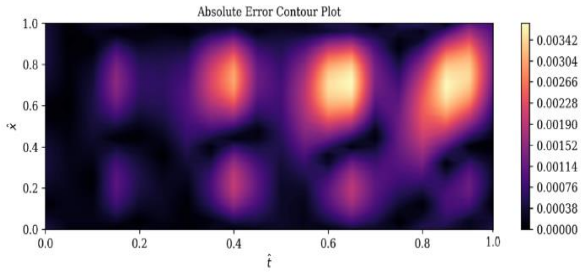

Figure 15. Absolute error in prediction PINNs & FEM $|w_{Pred} - w_{FEM}|$ for beam with variable cross section area ($\delta_2 = 0.5$)

The consequences of narrowing the beam with $\delta_3 = -0.5$ focus on describing the deflection of the beam during various bending stages, as shown in Figure 16. Observations indicate that the deflection shifts from the center towards the right, resulting in increased stiffness on one side of the beam. Consequently, the maximum deflection occurs on the stiffer side.

Furthermore, this configuration leads to an increase in the intensity of vibrations compared to beams with $\delta_1 = 0$. This increase is clearly visible in Figure 17, and when compared to the finite element method in Figure 18, it becomes evident that pins serve as a faster and more reliable solution, as the absolute error calculated in this case in Figure 19 is approximately 0.5%.

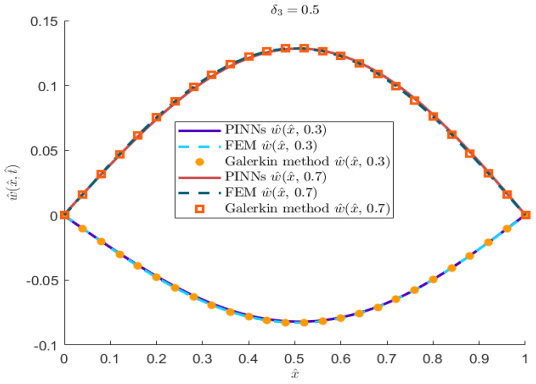

Figure 16. Forced vibration of beam with variable cross section area ($\delta_3 = -0.5$). comparison of the Galerkin, FEM and PINNs

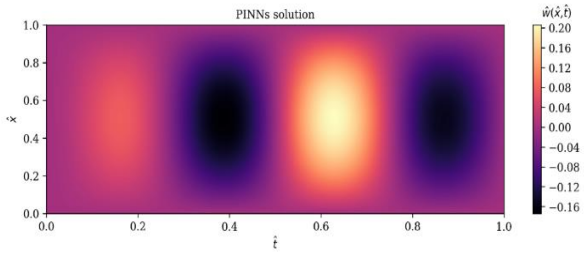

Figure 17. Transverse displacement of beam with constant cross section area ($\delta_3 = -0.5$). color bar represents PINNs solution

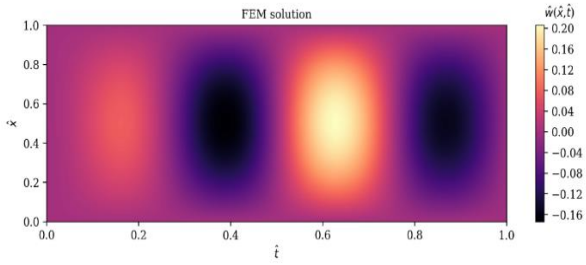

Figure 18. Transverse displacement of beam with constant cross section area ($\delta_3 = -0.5$). color bar represents FEM solution

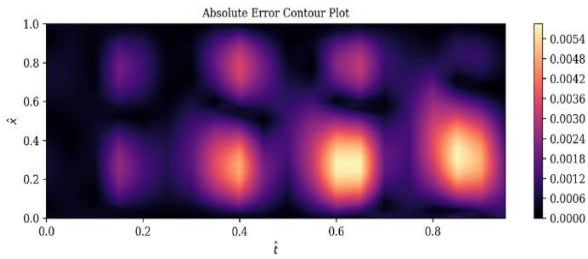

Figure 19. Absolute error in prediction PINNs & FEM $|w_{Pred} - w_{FEM}|$ for beam with variable cross section area ($\delta_3 = -0.5$)

6. CONCLUSIONS

In this study, physics-informed neural networks (PINNs) are used to formulate the equations of motion based on Euler-Bernoulli beam theory and Hamilton's principle to simulate the bending behavior of a beam with a variable cross-section. By applying boundary and initial conditions, a loss function is formulated, which allows for the smooth solution of partial differential equations (PDEs). The efficiency of physics-informed neural networks (PINNs) is evaluated by comparing its prediction accuracy with the results of data collected from the Galerkin and finite element methods. In all cases, the results obtained from the proposed physics-informed neural network (PINN) approach closely match the results obtained from the Galerkin and finite element methods. However, achieving the same level of accuracy as the Galerkin method requires a larger number of basics functions and the calculation of additional frequencies and finding mode shapes. For example, in this study, this problem was solved with a 6th-order Galerkin method. Finite element methods must first obtain the weak form of the equation after obtaining the differential equation, then obtain the stiffness, mass, and force matrices, and find a suitable mesh, which in this case consisted of 22 elements, and finally solve the system of equations with numerical methods such as the fourth-order Runge-Kutta method, which was used in this study, which significantly increases the computation time and the solution of a problem. In contrast, the time required for the proposed physics-informed neural network (PINN) framework is significantly shorter and provides results that match the accuracy of the Galerkin and finite element methods, even with a large number of basic functions. Therefore, expanding the application of physics-informed neural networks (PINNs) is essential to address more complex real-world problems. Furthermore, once trained, neural networks can quickly provide solutions at any given point with minimal additional computational effort. The most important results are summarized below:

1. It has been established that the PINNs Architecture, utilizing the specified Hyperparameters hidden layers configured as Neuron layers $N_h = 3$, $N_n = 100$, N_{pde}= 1000, N_{ic} = 200 and N_{bc}= 400, l_r = 0.1, Max- evaluations = $50k$, epochs = $15k$ Results obtained from the 6th-order Galerkin method and finite element method with 22 elements provide accurate and reliable predictions.
2. In forced vibrations, an increase in the delta value within the variable width causes one end of the beam to widen. This change creates a condition where one end of the beam has greater stiffness than the opposite end, resulting in a significant deviation from the center of the beam. Consequently, the overall distribution of forces within the beam changes, further amplifying the response to the occurrence of vibrations. In forced vibrations, an increase in the delta value in the variable width causes the beam end to widen and reduce the amplitude of vibrations.
3. In forced vibrations, decreasing delta in the beam width causes one end to become narrower than the other. This change in geometry increases the vibration amplitudes compared to a wider beam, leading to a non-uniform stress distribution that ultimately creates more pronounced oscillations under dynamic loads and results in greater stiffness in a portion of the system, with greater stiffness at one end of the beam.
4. Physics-informed neural networks (PINNs) effectively capture forced vibrations in beams with variable cross-sections. They provide solutions 45 times faster than the Galerkin method and 50 times faster than the finite element method, offering a highly efficient approach for analyzing complex beam behavior and facilitating faster design iterations.

7. REFERENCES

1. Elshafei MA. FE modeling and analysis of isotropic and orthotropic beams using first order shear deformation theory. Materials Sciences and Applications. 2013;4(1):77-102. https://doi.org/10.4236/msa.2013.41010
2. Thomsen DK, Søe-Knudsen R, Balling O, Zhang X. Vibration control of industrial robot arms by multi-mode time-varying input shaping. Mechanism and Machine Theory. 2021;155:104072. https://doi.org/10.1016/j.mechmachtheory.2020.104072
3. Li S, Shen L. Seismic optimization design and application of civil engineering structures integrated with building robot system technology. High-tech And Innovation Journal. 2024;5(4):1118-34. https://doi.org/10.28991/HIJ-2024-05-04-017
4. Makrup L, Pawirodikromo W, Muntafi Y. Comparison of structural response utilizing probabilistic seismic hazard analysis and design spectral ground motion. Civil Engineering Journal. 2024;10:235-51. https://doi.org/10.28991/CEJ-SP2024-010-012
5. Canales F, Mantari J. Free vibration of thick isotropic and laminated beams with arbitrary boundary conditions via unified formulation and Ritz method. Applied Mathematical Modelling. 2018;61:693-708. https://doi.org/10.1016/j.apm.2018.05.005
6. Moreno-García P, dos Santos JVA, Lopes H. A review and study on Ritz method admissible functions with emphasis on buckling and free vibration of isotropic and anisotropic beams and plates. Archives of Computational Methods in Engineering. 2018;25(3):785-815. https://doi.org/10.1007/s11831-017-9214-7
7. Azzara R, Carrera E, Filippi M, Pagani A. Vibration analysis of thermally loaded isotropic and composite beam and plate structures. Journal of Thermal Stresses. 2023;46(5):369-86. https://doi.org/10.1080/01495739.2023.2188399
8. Ghugal YM, Sharma R. A hyperbolic shear deformation theory for flexure and vibration of thick isotropic beams. International Journal of Computational Methods. 2009;6(04):585-604. https://doi.org/10.1142/S0219876209002017

9. Raissi M, Perdikaris P, Karniadakis GE. Physics-informed neural networks: A deep learning framework for solving forward and inverse problems involving nonlinear partial differential equations. Journal of Computational physics. 2019;378:686-707. https://doi.org/10.1016/j.jcp.2018.10.045
10. Namdeo J, Dubey S, Dorji L. Dynamic analysis of isotropic homogeneous beams using the method of initial functions and comparison with classical beam theories and FEM. Complexity. 2023;2023(1):6636975. https://doi.org/10.1155/2023/6636975
11. Zienkiewicz O, Taylor R, Ziaie-Moayed R, Kamalzare M, Safavian M, Zhou S, et al. Numerical Study of Floating Stone (static). Comput Geotech. 2013;2(2).
12. Kumar R, Tiwari R, Prasad R. Numerical solution of partial differential equations: finite difference method. Mathematics and Computer Science Volume 1. 2023:353-72. https://doi.org/10.2307/2007849
13. Lipnikov K, Manzini G, Shashkov M. Mimetic finite difference method. Journal of Computational Physics. 2014;257:1163-227. https://doi.org/10.1016/j.jcp.2013.07.031
14. Wang J, Wu R. The extended Galerkin method for approximate solutions of nonlinear vibration equations. Applied sciences. 2022;12(6):2979. https://doi.org/10.3390/app12062979
15. Polycarpou AC. Introduction to the finite element method in electromagnetics: Springer Nature; 2022.
16. Chen Z, Lai S-K, Yang Z. AT-PINN: Advanced time-marching physics-informed neural network for structural vibration analysis. Thin-Walled Structures. 2024;196:111423. https://doi.org/10.1016/j.tws.2023.111423
17. Bazmara M, Silani M, Mianroodi M, editors. Physics-informed neural networks for nonlinear bending of 3D functionally graded beam. Structures; 2023: Elsevier.
18. Bazmara M, Mianroodi M, Silani M. Application of physics-informed neural networks for nonlinear buckling analysis of beams. Acta Mechanica Sinica. 2023;39(6):422438. https://doi.org/10.1007/s10409-023-22438-x
19. Kapoor T, Wang H, Núñez A, Dollevoet R. Transfer learning for improved generalizability in causal physics-informed neural networks for beam simulations. Engineering Applications of Artificial Intelligence. 2024;133:108085. https://doi.org/10.1016/j.engappai.2024.108085
20. Kapoor T, Wang H, Núñez A, Dollevoet R. Physics-informed neural networks for solving forward and inverse problems in complex beam systems. IEEE Transactions on Neural Networks and Learning Systems. 2023;35(5):5981-95. https://doi.org/10.1109/TNNLS.2023.3310585
21. Söyleyici C, Ünver HÖ. A Physics-Informed Deep Neural Network based beam vibration framework for simulation and parameter identification. Engineering Applications of Artificial Intelligence. 2025;141:109804. https://doi.org/10.1016/j.engappai.2024.109804
22. Teloli RdO, Tittarelli R, Bigot M, Coelho L, Ramasso E, Le Moal P, et al. A physics-informed neural networks framework for model parameter identification of beam-like structures. Mechanical Systems and Signal Processing. 2025;224:112189. https://doi.org/10.1016/j.ymssp.2024.112189
23. Barillaro L. Deep learning platforms: PyTorch. 2025. https://doi.org/10.1016/B978-0-323-95502-7.00093-2
24. Vadyala SR, Betgeri SN, Betgeri NP. Physics-informed neural network method for solving one-dimensional advection equation using PyTorch. Array. 2022;13:100110. https://doi.org/10.1016/j.array.2021.100110
25. Chaudhary A, Chouhan KS, Gajrani J, Sharma B. Deep learning with PyTorch. Machine learning and deep learning in real-time applications: IGI Global; 2020. p. 61-95.
26. Hou Q, Li Y, Singh VP, Sun Z, Wei J. Physics-informed neural network for solution of forward and inverse kinematic wave problems. Journal of Hydrology. 2024;633:130934. https://doi.org/10.1016/j.jhydrol.2024.130934
27. Mehmood F, Ahmad S, Whangbo TK. An efficient optimization technique for training deep neural networks. Mathematics. 2023;11(6):1360. https://doi.org/10.3390/math11061360
28. Tong Q, Liang G, Cai X, Zhu C, Bi J. Asynchronous parallel stochastic Quasi-Newton methods. Parallel computing. 2021;101:102721. https://doi.org/10.1016/j.parco.2020.102721
29. Jagtap AD, Kawaguchi K, Karniadakis GE. Adaptive activation functions accelerate convergence in deep and physics-informed neural networks. Journal of Computational Physics. 2020;404:109136. https://doi.org/10.1016/j.jcp.2019.109136
30. Jagtap AD, Kawaguchi K, Em Karniadakis G. Locally adaptive activation functions with slope recovery for deep and physics-informed neural networks. Proceedings of the Royal Society A. 2020;476(2239):20200334. https://doi.org/10.1098/rspa.2020.0334

Persian Abstract

چکیده

این مطالعه به بررسی ارتعاشات اجباری تیرهای ایزوتروپیک با مقاطع متغیر می‌پردازد که بر مبنای نظریه تیر اویلر- برنولی مدلسازی شده است. با بهره‌گیری از اصل هامیلتون، معادلات دیفرانسیل حاکم بر دینامیک تیر استخراج شده و رفتارهای پیچیده ارتعاشی تحلیل می‌شوند.در این تحقیق، شبکه‌های عصبی مبتنی بر فیزیک (PINNs) به عنوان روشی نوآورانه و بدون نیاز به مش‌بندی، معرفی شده‌اند. این فناوری قادر است نتایج سریع و دقیقی را با تلفیق قوانین فیزیکی در فریمورک یادگیری ماشین ارائه کند. مزیت اصلی PINNs نسبت به روش‌های سنتی مانند اجزا محدود (FEM) یا روش‌های تفاضلی، ساده‌سازی فرآیند محاسباتی و کاهش زمان و منابع مورد نیاز است، زیرا دیگر نیاز به ساخت مش و تنظیم شبکه‌های پیچیده ندارد.نتایج به‌دست‌آمده . با استفاده از روش گالرکین مرتبه ششم واجزا محدود ، صحت و کارایی بالای این رویکرد را در تحلیل ارتعاشات تیرهای با مقاطع متغیر تأیید می‌کند. در مجموع، این پژوهش، کاربردهای PINNs در ارزیابی ارتعاشات را توسعه می‌دهد و در بهینه‌سازی طراحی و عملکرد در حوزه‌های مختلف مهندسی، از جمله سازه‌ها و سیستم‌های مکانیکی، نقش مؤثری ایفا می‌کند.